

# Amphipathic Binder Integrating Ultrathin and Highly Ion-Conductive Sulfide Membrane for Cell-Level High-Energy-Density All-Solid-State Batteries

Daxian Cao, Qiang Li, Xiao Sun, Ying Wang, Xianhui Zhao, Ercan Cakmak, Wentao Liang, Alexander Anderson, Soydan Ozcan, and Hongli Zhu\*

Current sulfide solid-state electrolyte (SE) membranes utilized in all-solid-state lithium batteries (ASLBs) have a high thickness (0.5–1.0 mm) and low ion conductance (<25 mS), which limit the cell-level energy and power densities. Based on ethyl cellulose's unique amphipathic molecular structure, superior thermal stability, and excellent binding capability, this work fabricates a freestanding SE membrane with an ultralow thickness of 47  $\mu\text{m}$ . With ethyl cellulose as an effective disperser and a binder, the  $\text{Li}_6\text{PS}_5\text{Cl}$  is uniformly dispersed in toluene and possesses superior film formability. In addition, an ultralow areal resistance of  $4.32 \Omega \text{ cm}^{-2}$  and a remarkable ion conductance of 291 mS (one order higher than the state-of-the-art sulfide SE membrane) are achieved. The ASLBs assembled with this SE membrane deliver cell-level high gravimetric and volumetric energy densities of  $175 \text{ Wh kg}^{-1}$  and  $675 \text{ Wh L}^{-1}$ , individually.

## 1. Introduction

Nowadays, safety issues and insufficient energy density (<250  $\text{Wh kg}^{-1}$ ) are two main concerns when applying commercial lithium-ion batteries (LiBs) to applications such as electric vehicles (EVs) and portable electronics.<sup>[1,2]</sup> All-solid-state lithium batteries (ASLBs) coupling solid-state electrolytes (SEs) with high-energy electrodes are considered as an effective

solution to overcome these two challenges.<sup>[3]</sup> Most SEs, especially the ceramic types, are incombustible, naturally nonvolatile, and have excellent thermal stability.<sup>[4]</sup> The employment of SEs would intrinsically address the thermal runaway caused by flammable organic liquid electrolytes in conventional LiBs. Additionally, SEs possessing a high elastic modulus were regarded to suppress the metallic anode Li metal dendrite growth.<sup>[5]</sup> The employment of Li metal can significantly boost the energy densities of the ASLBs. Furthermore, due to their solid state, SEs could enable the ASLBs a bipolar cell architecture, which would allow the cells to be stacked, further enhancing the energy

densities.<sup>[6,7]</sup> Thus, ASLBs are highly promising to achieve high safety and the desired energy densities (>500  $\text{Wh kg}^{-1}$  and >700  $\text{Wh L}^{-1}$ ) to meet the demand of EVs.<sup>[2]</sup>

However, most reported ASLBs delivered far lower energy densities (<50  $\text{Wh kg}^{-1}$  and <100  $\text{Wh L}^{-1}$ ) at the cell level.<sup>[8]</sup> This dramatic drop is mainly attributed to the utilization of thick electrolyte membranes. Note that the evaluation of cell-level energy density includes the masses and volumes of all parts of the batteries. In a sheet-type ASLB, an ideal SE membrane should concurrently have low areal resistance, high ion conductance, low thickness, high mechanical and chemical stability, and lightweight. The state-of-the-art membrane in LiBs with liquid electrolytes has a thickness of  $\approx 20 \mu\text{m}$ . In contrast, most reported solid inorganic electrolyte membranes show much higher thickness (0.5–1.0 mm).<sup>[9]</sup> These high thicknesses can not only dramatically reduce the cell-level energy density but also increase the internal resistance. Although some inorganic electrolytes, especially the sulfide SE, can exhibit a room-temperature ionic conductivity  $\sigma$  of  $>1.0 \text{ mS cm}^{-1}$ , the areal resistance  $R$  of the SE membrane is as high as  $100 \Omega \text{ cm}^2$ , calculated based on  $R = r * A = \frac{l}{\sigma}$ , where  $r$  is the resistance,  $A$  is

the area of the membrane,  $l$  is the thickness (we use 1 mm in this calculation), and  $\sigma$  is the conductivity. When further considering the interfacial resistance in cathode and anode, the internal resistance in ASLBs far exceeds the maximum limit of  $40 \Omega \text{ cm}^2$  proposed by Randau et al.<sup>[8]</sup> Therefore, to achieve cell-level high energy density and efficiency for practical application, the SE membrane must simultaneously possess a low thickness


D. Cao, Q. Li, X. Sun, Y. Wang, A. Anderson, H. Zhu  
Department of Mechanical and Industrial Engineering  
Northeastern University  
Boston, MA 02115, USA  
E-mail: h.zhu@neu.edu

X. Zhao, S. Ozcan  
Manufacturing Science Division  
Oak Ridge National Laboratory  
Oak Ridge, TN 37831, USA

X. Zhao  
Environmental Sciences Division  
Oak Ridge National Laboratory  
Oak Ridge, TN 37830, USA

E. Cakmak  
Materials Science and Technology Division  
Oak Ridge National Laboratory  
Oak Ridge, TN 37831, USA

W. Liang  
Kostas Advanced Nanocharacterization Facility (KANCF)  
Northeastern University  
Burlington, MA 01803, USA

 The ORCID identification number(s) for the author(s) of this article can be found under <https://doi.org/10.1002/adma.202105505>.

DOI: 10.1002/adma.202105505

and high ionic conductivity.<sup>[10]</sup> However, when reducing the thickness, the obtained membrane becomes brittle, which creates new challenges in both SE membrane fabrication and cell stability, like the short circuit of the ASLBs. It is challenging to fabricate an SE membrane with robust mechanical strength and a thin thickness (<50 μm).

Embedding sulfide SEs into a template and the binder-assisted methods, including solution casting and dry film fabrication, are the two most reported processes to fabricate thin SE membranes.<sup>[6]</sup> However, the ionic conductivities of the obtained membranes are generally reduced dramatically.<sup>[11]</sup> The template method is challenged by the ionic insulation of the template and insufficient infiltration of SE, which causes interrupted ion conduction paths and cavities, resulting in lower ionic conductivity. The chosen binders are critical to the membrane's ionic conductivity and mechanical strength for the binder-assisted methods. Considering that sulfide SEs are chemically unstable in polar solvents, the binders selected would ideally be soluble in nonpolar solvents, which is difficult for most binders. Conventional binder–solvent systems, like polyvinylidene fluoride (PVDF) in *N*-methyl-2-pyrrolidone (NMP), sodium carboxymethyl cellulose–styrene butadiene rubber (CMC–SBR) in water, polyacrylic latex in water, are not suitable for sulfide SE membrane fabrication. Owing to the good solubility in nonpolar xylene and considerable binding effect, rubbers, like SBR, silicon rubber (SR), and nitrile butadiene rubber (NBR), have enabled the fabrication of thin membranes with low thicknesses through a slurry-coating approach.<sup>[12]</sup> However, the ionic conductivities are not satisfactory (<1 mS cm<sup>-1</sup>) in these works. One of the major reasons is that the binders wrapped the ionic conductive ceramic powders and blocked the ion conduction paths. Therefore, on the one hand, the fraction of binder should be minimized to help the membrane maintain high ionic conductivity. On the other hand, the mechanical strength of the SE membrane will be challenging when the binder amount and the membrane thickness are greatly reduced. Thus, a strong binding between binder and sulfide SE is necessary. Therefore, developing advanced binders is important to prepare ultrathin, robust, and highly ion-conductive membranes.

In this work, for the first time, ethyl cellulose was employed as a disperser and a binder during electrolyte suspension preparation and SE membrane fabrication. Cellulose is the most abundant biopolymer on the earth.<sup>[13]</sup> Ethyl cellulose is a derivative of cellulose through an etherification reaction, through which a certain amount of hydrophilic hydroxyl groups is converted into oleophilic ethyl groups.<sup>[14]</sup> The resultant ethyl cellulose shows unique properties, including excellent solubility in nonpolar organic solvents, excellent dispersing capability, outstanding film formability, and high binding strength. These properties enable ethyl cellulose in applications such as food packaging, drug delivery, and emulsion fabrication.<sup>[14,15]</sup> The high mechanical tensile strength of 47–72 MPa of ethyl cellulose benefits the robustness when compositing it with other materials.<sup>[16]</sup> Inspired by these merits, we utilized ethyl cellulose to prepare the thin SE membrane. As a result, a free-standing, ultrathin, robust, and highly ion-conductive sulfide SE membrane was successfully fabricated based on the argyrodite Li<sub>6</sub>PS<sub>5</sub>Cl electrolyte. Through a scalable vacuum filtration process, the thickness of the membrane was well controlled. In

addition, we also investigated the excellent chemical and electrochemical compatibility of ethyl cellulose with both Li<sub>6</sub>PS<sub>5</sub>Cl and toluene. More importantly, the ethyl cellulose is discretely distributed inside the SE membrane instead of continuous wrapping, which was well defined through X-ray computed tomography (XCT). Li<sub>3</sub>InCl<sub>6</sub> is used as the ion conductor in the cathode layer due to its high stability with LiCoO<sub>2</sub> and Li<sub>6</sub>PS<sub>5</sub>Cl. The ASLB produced by coupling this advanced SE and stabilized cathode displayed a high cell-level energy density for practical applications.

## 2. Results and Discussion

It is essential to employ a thin SE membrane in the ASLB with high energy densities. Compared to the conventional cold press method, the binder-assisted solution method can efficiently fabricate a thin SE membrane, and it is scalable. However, the binder must meet the following requirements: 1) high chemical compatibility with both ceramic ion conductors and solvent; 2) excellent thermal stability during high temperature (≈200 °C) treatment to remove solvent; 3) superior mechanical binding strength; 4) excellent film formability; and 5) negligible adverse effects on ion conduction.

**Figure 1A** illustrates the required compatibility among sulfide SE, binder, and solvent in the thin SE membrane fabrication through the solution method. As aforementioned, a nonpolar solvent is necessary to avoid the reaction with sulfide SE. The binder with oleophilic groups is suggested due to their better solubility in a nonpolar solvent. Since a uniformly dispersed slurry is crucial in the thin film fabrication, a weak bonding between SE and binder, like the van der Waals forces, will benefit the dispersion uniformity of SE in the nonpolar organic solvent. Therefore, the binder is desired with multifunction. Moreover, the thermal stability of the binder is essential in film fabrication, as illustrated in **Figure 1B**. Because an additional heating process (temperature > 200 °C) was generally employed to thoroughly remove the solvent in the membrane, the binder would ideally have high thermal stability to maintain the structure and binding capability. The thermal degradation of binders at elevated temperatures causes cracks and defects in the membrane and ionic conductivity deterioration. In addition, the distribution of the binder effectively impacts the membrane's ionic conductivity, as depicted in **Figure 1C**. Considering that most of the binders are nonion conductive, the binder may block the ion conduction if it completely wrapped the sulfide SE. The ideal protocol is that the ion conductor is continuous, and the binder is randomly distributed inside the SE membrane to guarantee continuous ion conduction paths. Therefore, it is vital to minimize the binder amount, which challenges the mechanical strength of the membrane. **Figure 1D** describes the effect of the binding ability of the binder on the mechanical strength of the membrane. The weak binding will cause poor mechanical strength and limit the application of a thin SE membrane. A strong binding can enhance mechanical stability, especially with a low amount of binder.

Different polymers were tested and screened in this work, including regular cellulose, 2,2,6,6-tetramethylpiperidine-1-oxyl (TEMPO) oxidized cellulose nanofiber grafted with polyethylene

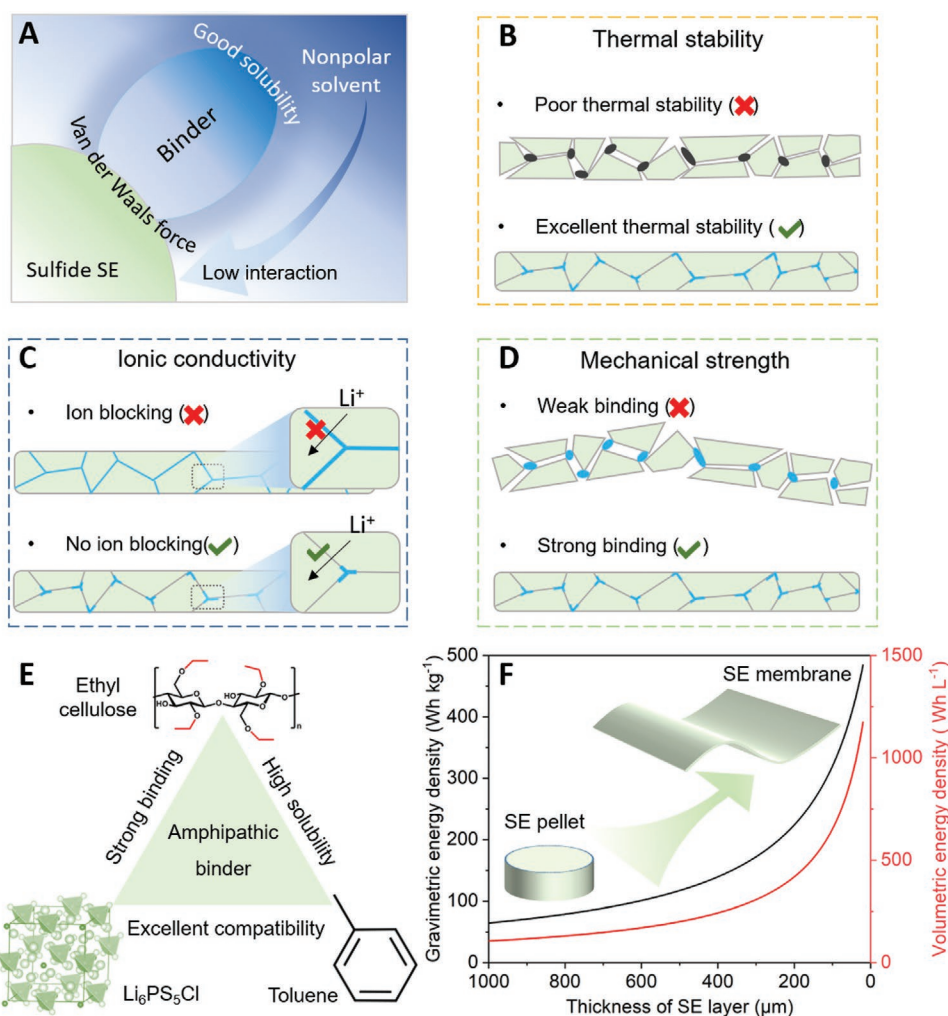


**Figure 1.** Overview of this work. A) Illustration of compatibility among sulfide SE, binder, and solvent. Schematic to display the effect of binder on B) thermal stability, C) ionic conductivity, and D) mechanical strength of the SE membrane. E) Illustration of compatibility among  $\text{Li}_6\text{PS}_5\text{Cl}$ , ethyl cellulose, and toluene in thin membrane fabrication. F) Estimated gravimetric and volumetric energy densities of ASLBs as the factor of the thickness of SE layers in ASLB coupling  $\text{LiCoO}_2$  and Li metal.

glycol, and flax fiber, but all of them show poor dispersion and film formability when compositing with  $\text{Li}_6\text{PS}_5\text{Cl}$  (Figures S1 and S2, Supporting Information) in toluene. In contrast, ethyl cellulose with the oleophilic ethyl groups has excellent solubility in toluene, as presented in Figure S3 (Supporting Information). The amphipathic property (oleophilic of ethyl groups and hydrophilic of hydroxyl groups) of ethyl cellulose enables a uniform and stable dispersion of ethyl cellulose with sulfide SE in toluene-like surfactant. Meanwhile, the remained hydroxyl groups on ethyl cellulose form a mild bonding with sulfide SE due to the interaction of the negative hydroxyl groups with positive electron-accept sites, such as  $\text{P}^{5+}$  and  $\text{Li}^+$ . Moreover, the strong binding and excellent film formability of ethyl cellulose enable the thin membrane formation with considerable mechanical strength even at a low ratio (2 wt%). In addition, owing to the excellent thermal stability over 200 °C (as shown in Figure S4 of the Supporting Information), ethyl cellulose could survive in the high-temperature solvent removal process. Ultimately, ethyl cellulose was selected based on its unique

amphipathicity, mechanical binding strength, and excellent thermal stability. Figure 1E illustrates the compatibility among  $\text{Li}_6\text{PS}_5\text{Cl}$ , ethyl cellulose, and toluene in this process.  $\text{Li}_6\text{PS}_5\text{Cl}$  is a widely studied sulfide SE due to its outstanding ionic conductivity ( $\approx 1.6 \text{ mS cm}^{-1}$ ), facile synthesis, and low cost. Furthermore,  $\text{Li}_6\text{PS}_5\text{Cl}$  shows excellent stability when dispersed in toluene due to the low polarity of toluene (0.099 of relative polarity),<sup>[17]</sup> resulting in excellent compatibility and an intact ionic conductivity after treatment. Thus, the system using  $\text{Li}_6\text{PS}_5\text{Cl}$ , ethyl cellulose, and toluene enables the successful fabrication of a thin SE membrane owing to high ionic conductivity and mechanical strength at the same time.

The employment of a thin SE membrane could significantly boost the energy densities of the ASLB. Figure 1F displays the estimated cell-level gravimetric and volumetric energy densities (including cathode, anode, and electrolyte) as the factors of the thickness of the SE membrane in a typical sheet-type ASLB coupling  $\text{LiCoO}_2$  and Li metal. The detailed information used for the estimation is listed in Table S1 (Supporting

Information). As the SE membrane thickness varies from 1000 to 20  $\mu\text{m}$ , both gravimetric and volumetric energy densities are dramatically increased from 65  $\text{Wh kg}^{-1}$  and 106  $\text{Wh L}^{-1}$  to 484  $\text{Wh kg}^{-1}$  and 1174  $\text{Wh L}^{-1}$ , respectively. Thus, compared to the SE pellet with high thickness, the thin SE membrane contributes a lightweight and higher energy density, and a reduced internal resistance resulting in enhanced energy storage efficiency in ASLBs.

The unique amphipathic molecular structure of ethyl cellulose enables the fabrication of a thin and robust membrane. **Figure 2A** shows the dispersions of  $\text{Li}_6\text{PS}_5\text{Cl}$  in toluene with and without ethyl cellulose after standing for 1 h. The  $\text{Li}_6\text{PS}_5\text{Cl}$  is uniformly dispersed in toluene with the addition of 2.0 wt% ethyl cellulose. In contrast, there are apparent precipitations in the sample with no ethyl cellulose but only  $\text{Li}_6\text{PS}_5\text{Cl}$ . The enhanced dispersion stability is highly related to the amphipathic molecular structure of ethyl cellulose. Compared with conventional cellulose, ethyl cellulose has partially substituted hydroxyl groups with ethyl groups (**Figure 2B**). As shown in attenuated total reflection Fourier-transform infrared spectroscopy (ATR-FTIR), cellulose had a well-defined peak centered at around 3500  $\text{cm}^{-1}$ , attributed to its abundant hydroxyl groups. However, the peak at this wavenumber is much weaker for ethyl cellulose since the ethyl groups substituted the hydroxyl groups (degree of substitution was at 2.5). This substitution is also evidenced by the weaker peak of ethyl cellulose at 1430  $\text{cm}^{-1}$  than cellulose, assigned to in-plane bending of  $-\text{OH}$  in the glucose unit. In the meantime, the peak at 1375  $\text{cm}^{-1}$  assigned to  $-\text{CH}_3$  bending presents for ethyl cellulose other than cellulose, attributed to the methyl end groups in the ethyl moieties of ethyl cellulose. We also found an asymmetric peak at around 2950–2850  $\text{cm}^{-1}$  for ethyl cellulose, assigned to  $-\text{CH}$  stretching as reported.<sup>[18]</sup> The hydrophobic branches in ethyl cellulose have enabled its outstanding solubility in toluene.

To further evaluate the dispersion uniformity and interaction of  $\text{Li}_6\text{PS}_5\text{Cl}$  with ethyl cellulose in toluene, the viscosities of cellulose, ethyl cellulose,  $\text{Li}_6\text{PS}_5\text{Cl}$ ,  $\text{Li}_6\text{PS}_5\text{Cl}$ –cellulose, and  $\text{Li}_6\text{PS}_5\text{Cl}$ –ethyl cellulose are compared in **Figure 2C**. The dispersion of  $\text{Li}_6\text{PS}_5\text{Cl}$ –ethyl cellulose shows significantly higher viscosity than that of single components, suggesting that excellent bonding exists between  $\text{Li}_6\text{PS}_5\text{Cl}$  and ethyl cellulose. Ethyl cellulose owns a negative charge on the surface derived from the remaining hydroxyl groups.<sup>[19]</sup> Meanwhile, the phosphorus and Li ions in  $\text{Li}_6\text{PS}_5\text{Cl}$  act as electron acceptors to interact with ethyl cellulose and generate bonding.<sup>[20]</sup> This bonding helps the stable dispersion of  $\text{Li}_6\text{PS}_5\text{Cl}$  in toluene but is not strong enough to cause the degradation of  $\text{Li}_6\text{PS}_5\text{Cl}$ .

After preparing the well-dispersed  $\text{Li}_6\text{PS}_5\text{Cl}$  suspension, a vacuum filtration process was applied to fabricate a thin membrane, as shown in **Figure 2D**. The obtained freestanding membrane was further cold-pressed into an ultrathin and dense layer for future use. In addition to the abovementioned bonding, ethyl cellulose also exhibits a strong binding effect with  $\text{Li}_6\text{PS}_5\text{Cl}$  enabling the SE membrane to be peeled off from the filter paper after filtration. As a result, the ion conduction paths in the thin SE membrane can remain continuous without being blocked. Therefore, the thin membrane simultaneously

achieves an intact ionic conductivity and considerable mechanical robustness.

**Figure 2E** displays the as-prepared freestanding SE membrane. There are no cracks after the membrane being peeled off from the filter paper. In contrast to the conventional SE pellet with a diameter of <1.3 cm, the SE membrane has a diameter of 44 mm. Employing a larger filtration setup can further scale up the sample size. For comparison, the sample prepared with the same process but without ethyl cellulose shows poor film formability where the membrane pulverizes after removing the solvent (**Figure 2F**). The SE membrane can be further punched into smaller sizes without fracturing, as shown in **Figure S5** (Supporting Information), suggesting outstanding robustness. The as-punched SE membrane with a diameter of 1.27 cm also shows considerable flexibility, as shown in **Figure 2G**, benefiting the following ASLB fabrication process. The areal weight of the SE membrane was as low as 79  $\text{mg cm}^{-2}$ . **Figure 2H** shows the conventional SE pellet prepared through the cold press. The areal weight is as high as 158.7  $\text{mg cm}^{-2}$ , 20 times higher loading compared to the thin SE membrane. The thickness of the SE membrane before pressing is 180  $\mu\text{m}$ . After pressing at 300 MPa, the thickness decreases to 47  $\mu\text{m}$  (**Figure 2I**). In comparison, a regular SE pellet exhibits a much higher thickness of 976  $\mu\text{m}$ .

Considering that the SE membrane generally experiences a high pressure in ASLB, robustness under compression is necessary to avoid mechanical failure. **Figure 2J** displays the stress–strain profile of a thin SE membrane in an axial compression process. It suggests that the thin SE membrane experiences three stages: elastic deformation, plastic deformation, and densification, similar to the behavior of the porous wood sample.<sup>[21]</sup> The SE membrane does not show fracturing even at high compression stress of 80 MPa, although a high deformation is observed (90% reduction in thickness). In contrast, the thick SE pellet shows an obvious fracture point at low stress of 0.27 MPa (**Figure 2K**). Overall, the introduction of ethyl cellulose significantly improves the membrane robustness in the compression process attributing to the strong binding ability of ethyl cellulose with  $\text{Li}_6\text{PS}_5\text{Cl}$ .

The tensile strength of the thin SE membrane is also investigated, as shown in **Figure S6** (Supporting Information). The thin SE membrane shows a high tensile strength of 495 kPa and a high Young's modulus of 12.56 MPa. The excellent mechanical strength demonstrates that the thin SE membrane owns good processability in fabricating ASLBs.

**Figure 3A** displays the cross-sectional scanning electron microscopy (SEM) image of the freestanding thin SE membrane. As highlighted by the yellow dash lines, the membrane shows a uniform thickness of around 50  $\mu\text{m}$ , and no apparent voids or cracks are observed. The energy dispersive X-ray spectroscopy (EDS) mapping in **Figure 3B** confirms the homogeneously distributed Cl, S, and P elements from  $\text{Li}_6\text{PS}_5\text{Cl}$ . In the magnified images in **Figures 3C,D**, the  $\text{Li}_6\text{PS}_5\text{Cl}$  particles smaller than 3  $\mu\text{m}$  are closely stacked together to form a dense membrane. The ethyl cellulose is not visible on the surface or interface between  $\text{Li}_6\text{PS}_5\text{Cl}$  particles, avoiding the ion conduction block caused by the ethyl cellulose that wraps the  $\text{Li}_6\text{PS}_5\text{Cl}$  particles. **Figure 3E** shows the top view of the membrane where there are no apparent voids or cracks. The



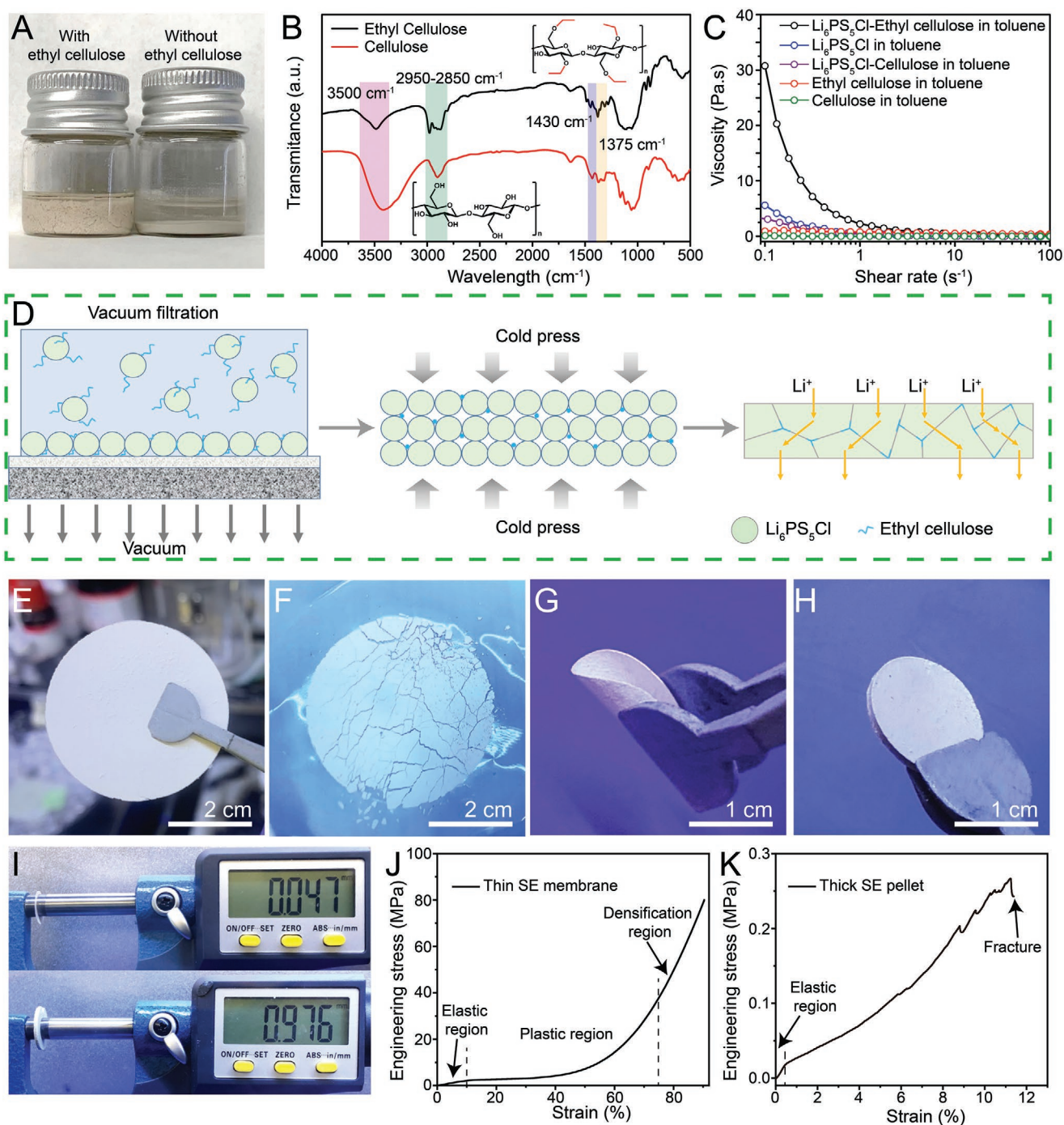


**Figure 2.** Fabrication of the thin SE membrane. A) Photo of the  $\text{Li}_6\text{PS}_5\text{Cl}$  dispersions in toluene with/without ethyl cellulose. B) FTIR spectra of ethyl cellulose and cellulose. Insets are chemical structures of ethyl cellulose and regular cellulose individually. C) Viscosity as a function of the shear rate for various dispersions or solutions:  $\text{Li}_6\text{PS}_5\text{Cl}$ -ethyl cellulose in toluene,  $\text{Li}_6\text{PS}_5\text{Cl}$  in toluene,  $\text{Li}_6\text{PS}_5\text{Cl}$ -cellulose in toluene, ethyl cellulose in toluene, and cellulose in toluene. D) Schematic of the binder-assisted vacuum filtration method in fabricating the thin SE membrane. Photos of E) the thin SE membrane composed of  $\text{Li}_6\text{PS}_5\text{Cl}$  and ethyl cellulose, F) the thin SE membrane with only  $\text{Li}_6\text{PS}_5\text{Cl}$ , G) bent thin SE membrane to show the flexibility, and H) thick SE pellet. I) Photos of the thin SE membrane and thick SE pellet in thickness measurement. Stress-strain profiles of J) thin SE membrane and K) thick SE pellet in an axial compression process.

uniform thickness and homogeneous distribution originate from the highly stable dispersion of  $\text{Li}_6\text{PS}_5\text{Cl}$ -ethyl cellulose in toluene and the efficient solvent removal in the vacuum filtration process.

As aforementioned, the  $\text{Li}_6\text{PS}_5\text{Cl}$  is highly sensitive to many polar solvents and binders. Herein the stabilities of  $\text{Li}_6\text{PS}_5\text{Cl}$  against toluene and ethyl cellulose were investigated. Figure 3F compares X-ray diffraction (XRD) patterns of

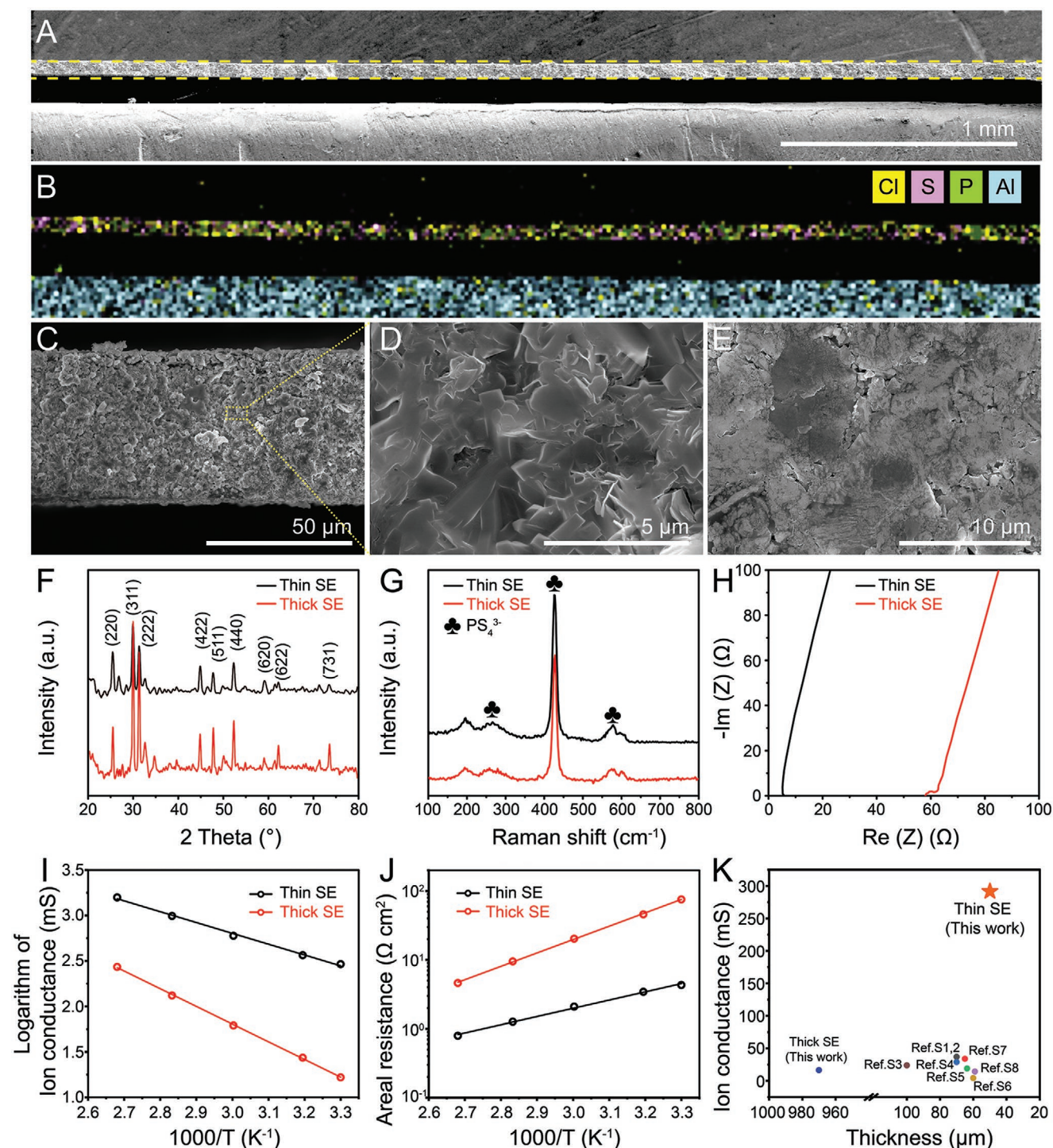


**Figure 3.** Performance of the thin SE membrane. A) Cross-sectional SEM image and B) EDS mapping of the thin SE membrane. The cross-sectional SEM images of thin SE membrane with magnitudes of C)  $\times 1k$  and D)  $\times 10k$ . E) The surface morphology of the thin SE membrane from the top view. F) XRD patterns and G) Raman spectra of the thin and thick SEs. H) Nyquist plots in AC impedance measurement of the thin and thick SEs. The temperature-dependent I) ion conductance and J) areal resistances of the thin and thick SEs. K) Comparison of the ion conductance at 30 °C of this SE membrane with other reported sulfide thin SE membranes.

a thin SE membrane prepared with ethyl cellulose in toluene through wet filtration and a thick SE pallet without ethyl cellulose fabricated with dry pressing in the range from 20° to 80°. There are no newborn peaks and peak position shifts observed

in thin SE compared with thick SE, indicating excellent compatibility between  $Li_6PS_5Cl$  with ethyl cellulose and toluene. All the patterns are indexed to the typical argyrodite (cubic space group:  $F-43m$ ). The prominent diffraction peaks at 25.5°, 30.0°,



31.4°, 45.0°, 47.9°, and 52.4° are indexed to (220), (311), (222), (422), (511), and (440) planes, respectively.<sup>[22]</sup> The Raman spectra of both thin SE and thick SE are displayed in Figure 3G to confirm that the fabrication process has no damage to Li<sub>6</sub>PS<sub>5</sub>Cl. The peaks located at 195.9, 263.3, 426.7, 577.8, and 600.5 cm<sup>-1</sup> are attributed to the tetrahedral PS<sub>4</sub><sup>3-</sup> unit in argyrodite-type Li<sub>6</sub>PS<sub>5</sub>Cl.<sup>[23]</sup> As a result, the membrane fabrication process shows the marginal side effect on Li<sub>6</sub>PS<sub>5</sub>Cl, which is necessary for achieving high ionic conductivity.

The ionic conductivities of the thin SE and thick SE were evaluated through an AC impedance measurement in a symmetric cell with ion-blocking electrodes. Figure 3H compares the amplified Nyquist plots of thin SE and thick SE at high and mid frequencies at 30 °C. The thin SE and thick SE thicknesses used in the measurement are 52 and 970 μm, respectively. Both SEs exhibited a typical diagram of sulfide superconductors where the plots are mainly a straight line demonstrating superior ionic conductivity. Neglecting the resistance from the external circuit, the overall ionic resistance of the SE is the sum of the bulk resistance, grain boundary resistance, and external resistance. The external resistance stemming from the outer wires and packages of the cell is measured as 1.83 Ω and subtracted in the ion conductivity evaluation (Figure S7, Supporting Information). Impressively, the thin SE had an ultralow resistance of 3.43 Ω and a high ionic conductivity of 1.65 mS cm<sup>-1</sup>, comparable to the intrinsic ionic conductivity of Li<sub>6</sub>PS<sub>5</sub>Cl. More importantly, the derived ion conductance is as high as 291.55 mS, representing the highest value reported so far. In contrast, the thick SE exhibits a much higher resistance of 60.37 Ω. Though the ionic conductivity is as high as 1.67 mS cm<sup>-1</sup>, the ion conductance is only 16.62 mS. Therefore, a tenfold increase in ion conductance is achieved by reducing the thickness of the SE.

The ion conduction of thin and thick SEs at various temperatures (from 30 to 100 °C) were investigated (details in Table S2 of the Supporting Information). The temperature affects the ionic conductivity, which is related to the activation energy of SEs. As shown in Figures S8 and S9 (Supporting Information), the plots shift to the left at higher temperatures indicating enhanced ion conduction. Figure 3I compares the temperature-dependent ion conductance of thin and thick SEs. The ion conductance of thick SE varies more than that of thin SE as temperature increases. There is an increase of over 16-fold from 16.62 to 272.48 mS in ion conductance of thick SE, attributed to an activation energy of 0.416 eV. In contrast, the thin SE delivers a slight increase in ion conductance from 291.55 to 1587.30 mS, resulting in an activation energy of 0.264 eV. The causes of significant differences in activation energy are still under investigation. Notably, the ion conductance of thin SE at 30 °C (291.55 mS as mentioned above) is even higher than that of thick SE at 100 °C (272.48 mS), although the ionic conductivity of thin SE is much lower than that of thick SE (1.65 mS cm<sup>-1</sup> at 30 °C for thin SE and 27.44 mS cm<sup>-1</sup> at 100 °C for thick SE). The dramatically enhanced ion conductance was contributed to the significantly reduced thickness (from 970 to 50 μm) and only very slightly sacrificed ionic conductivity (from 1.67 to 1.65 mS cm<sup>-1</sup>). Moreover, the areal resistances of thin and thick SEs were evaluated to have a normalized comparison, as displayed in Figure 3J. The thin SE has an ultralow

areal resistance of 4.32 Ω cm<sup>2</sup> at 30 °C, while the thick SE exhibits a much higher value of 60.17 Ω cm<sup>2</sup>. Excluding the charge-transfer resistances, the thin SE is promising to enable the ASLB with an internal resistance lower than the demanded 40 Ω cm<sup>2</sup>. Figure 3K compares the ion conductance of SE membranes in this work with other reported values (details in Table S3 of the Supporting Information). This thin SE membrane has the highest ion conductance among various thin-film SEs.

To further highlight the significance of ethyl cellulose, we prepared the thin film using regular cellulose as a binder through the same processes. Due to the richness in hydrophilic hydroxyl groups, regular cellulose exhibits poor dispersion in toluene even after mechanical pulverization. The dispersion of Li<sub>6</sub>PS<sub>5</sub>Cl and cellulose quickly precipitates after standing for 1 min (Figure S10, Supporting Information). After filtration, the samples with a cellulose ratio of <10 wt% showed poor film formability, attributed to the poor binding effect between cellulose and Li<sub>6</sub>PS<sub>5</sub>Cl. We then obtained a freestanding membrane with 10 wt% of cellulose, and it broke into pieces when peeled off from the filter paper due to poor mechanical strength (Figure S11, Supporting Information). An incomplete circular membrane with a low thickness of 64 μm was fabricated after being cold-pressed at 300 MPa. The ionic conductivity was only 0.12 mS cm<sup>-1</sup>, which agreed well with other fiber-reinforced thin SE membranes prepared by cold pressing (Figure S12, Supporting Information).<sup>[24]</sup> In this sample, because of poor binding with Li<sub>6</sub>PS<sub>5</sub>Cl, fibrous cellulose acted as the building block but not as a binder in film fabrication. A high fraction of cellulose fibers was desired to maintain a good mechanical strength but may block the ion conduction in the membrane and reduce the ionic conductivity.

The ion conduction pathways are significantly determined by the distributions of Li<sub>6</sub>PS<sub>5</sub>Cl, ethyl cellulose, and pores. Therefore, the XCT is employed to study the distribution of Li<sub>6</sub>PS<sub>5</sub>Cl, ethyl cellulose, and pores. Unlike SEM, which only provides surface information, XCT is a powerful technique to probe internal structure and generate 3D reconstructions based on the segmental scans.<sup>[25]</sup> Figure 4A shows the 2D image of the thin SE membrane from the top view. There are obvious gray level contrasts in different regions because of the density differences of the compositions. The bright region represents the Li<sub>6</sub>PS<sub>5</sub>Cl which is heaviest, and the dark gray region is attributed to relatively lighter ethyl cellulose, and the black spots are the pores. Figure 4B highlights the distribution of Li<sub>6</sub>PS<sub>5</sub>Cl with yellow color. Notably, Li<sub>6</sub>PS<sub>5</sub>Cl takes the main fraction of the thin SE membrane and forms an integrated region, which benefits ion conduction. The regions with red color in Figure 4C correspond to the ethyl cellulose, which scatteringly distributes in the SE membrane and does not form continuous wrapping. There are also pores detected in the thin membrane, labeled as blue in Figure 4D. It is interesting that pore locations are accompanied by the ethyl cellulose regions. Figure 4E displays the magnified 2D image of the SE membrane. The Li<sub>6</sub>PS<sub>5</sub>Cl shows two different gray levels agreeing with the previous results.<sup>[26]</sup> The particle size in the bright region is much larger than that in the gray region. The loose packing of the small particles could result in a lower X-ray absorption delivering a gray color. In Figure 4F, the Li<sub>6</sub>PS<sub>5</sub>Cl owns a high calculated volume fraction

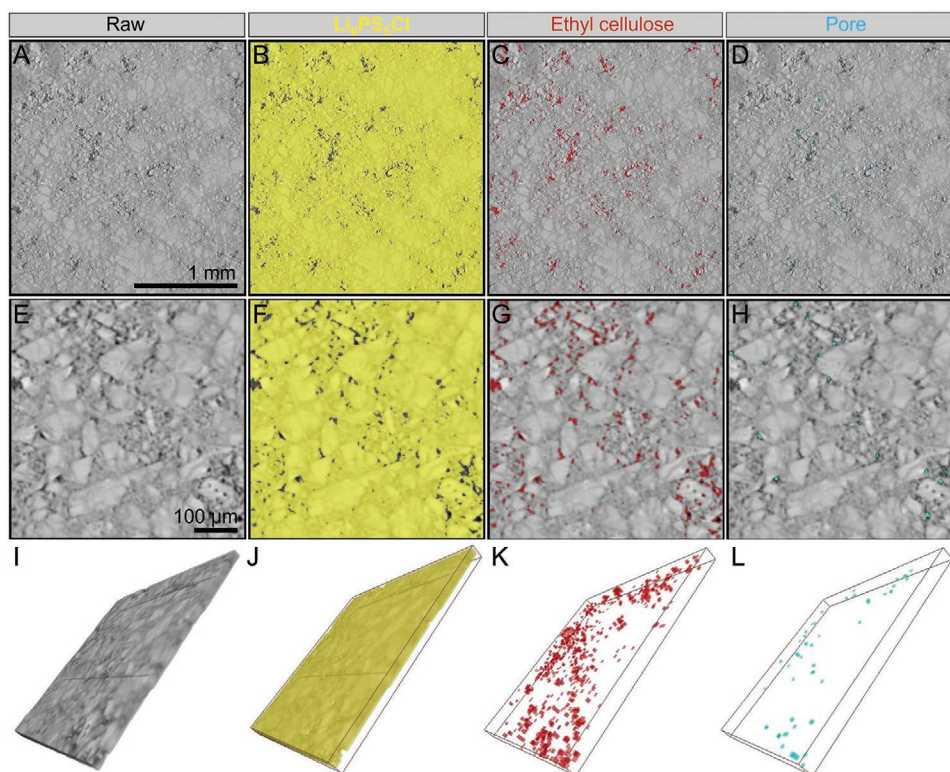


**Figure 4.** Distribution of  $\text{Li}_6\text{PS}_5\text{Cl}$  and ethyl cellulose in thin SE membrane revealed by X-ray computed tomography. A) Reconstructed 2D images of the thin SE membrane in the surface and the distribution of B)  $\text{Li}_6\text{PS}_5\text{Cl}$  labeled with yellow color, C) ethyl cellulose marked with red color, and D) pores tagged with blue color. E) Magnified surface images of the thin membrane and the distribution of F)  $\text{Li}_6\text{PS}_5\text{Cl}$  labeled with yellow color, G) ethyl cellulose marked with red color, and H) pores labeled with blue color. I) 3D segmented image of a  $500 \times 500 \times 50 \mu\text{m}$  subvolume of the thin SE membrane, and the renderings to show the distribution of J)  $\text{Li}_6\text{PS}_5\text{Cl}$  labeled with yellow color, K) ethyl cellulose tagged with red color, and L) pores marked with blue color.

of 96.986 vol% and shows continuous connections evidencing the high ionic conductivity. Figure 4G highlights the distribution of ethyl cellulose in the SE membrane. The ethyl cellulose randomly distributes at the boundaries of  $\text{Li}_6\text{PS}_5\text{Cl}$  particles but not fully wrapping the  $\text{Li}_6\text{PS}_5\text{Cl}$  particles contributing to less barrier and more continuous ion-transport paths. The volume fraction of ethyl cellulose is 2.92 vol%. In Figure 4H, there are also pores observed, and the volume fraction is as low as 0.094 vol%. The pores' generation is inevitable in solid electrolyte membrane, and the porosity can reach 23% in the cold-pressed pellet using  $\text{Li}_6\text{PS}_5\text{Cl}$  powders under the pressure of 370 MPa.<sup>[27]</sup> Therefore, the addition of ethyl cellulose enables the thin SE membrane with lower pores benefiting the ion conduction. Furthermore, Figure 4I displays the 3D segmented image of a  $300 \times 300 \times 50 \mu\text{m}$  subvolume of the thin SE membrane. No huge cracks or voids are observed in the crosssection. In the 3D segmented rendering of  $\text{Li}_6\text{PS}_5\text{Cl}$  (Figure 4J), we can see that the distribution of ion conductors in the whole membrane is continuous, which guarantees the high ionic conductivity of the whole composite membrane. Figure 4K illustrates 3D segmented rendering of ethyl cellulose, which exists as the point and is scatteringly distributed in this subvolume. In Figure 4L, Sporadic pores are also observed, demonstrating the thin SE membrane owning high density.

In ASLBs, the cathode layer plays an equally significant role with the thin SE in boosting the energy density.

Generally, the cathode layer comprises active material, SEs, and other components like carbon additives and binders. Benefiting from the high working voltage ( $>3.9 \text{ V}$ ), impressive capacity ( $>200 \text{ mAh g}^{-1}$ ), and considerable electron conductivity ( $\approx 10^{-5} \text{ S cm}^{-1}$ ), lithium cobalt oxide ( $\text{LiCoO}_2$ ) has attracted numerous attentions.<sup>[28]</sup> However, sulfide SEs suffer from poor stability with  $\text{LiCoO}_2$ , resulting in an interface passivation layer formation with sluggish ion conduction, as illustrated in Figure 5A. Surface coating layers, such as  $\text{LiNbO}_3$  and  $\text{Li}_{0.35}\text{La}_{0.5}\text{Sr}_{0.05}\text{TiO}_3$ , have been reported to stabilize the interface between sulfide SEs and oxide cathodes.<sup>[23,29]</sup> However, the commonly relatively low ionic conductivity ( $10^{-9}$ – $10^{-6} \text{ S cm}^{-1}$ ) of coating material rendered a new interface resistance. The high cost also constricts the large-scale application. Meanwhile, it is challenging to coat a uniform and thin layer with scalable methods for industrial application. To address this challenge, a halide superionic conductor,  $\text{Li}_3\text{InCl}_6$ , was employed as the SE in the cathode layer. The as-prepared  $\text{Li}_3\text{InCl}_6$  shows an ionic conductivity of  $0.4 \text{ mS cm}^{-1}$  (Figure S13, Supporting Information). The  $\text{Li}_3\text{InCl}_6$  was reported with high oxidation potential (up to 6.0 V), excellent chemical stability against  $\text{LiCoO}_2$ , and natural softness to achieve intimate contact with  $\text{LiCoO}_2$ .<sup>[30]</sup> As depicted in Figure 5B, a stable interface with fast ion transfer is formed without additional interface coating. The  $\text{LiCoO}_2$ – $\text{Li}_3\text{InCl}_6$  mixture was prepared through a facile water-mediated process.<sup>[31]</sup> Figure 5C compares the XRD spectra of



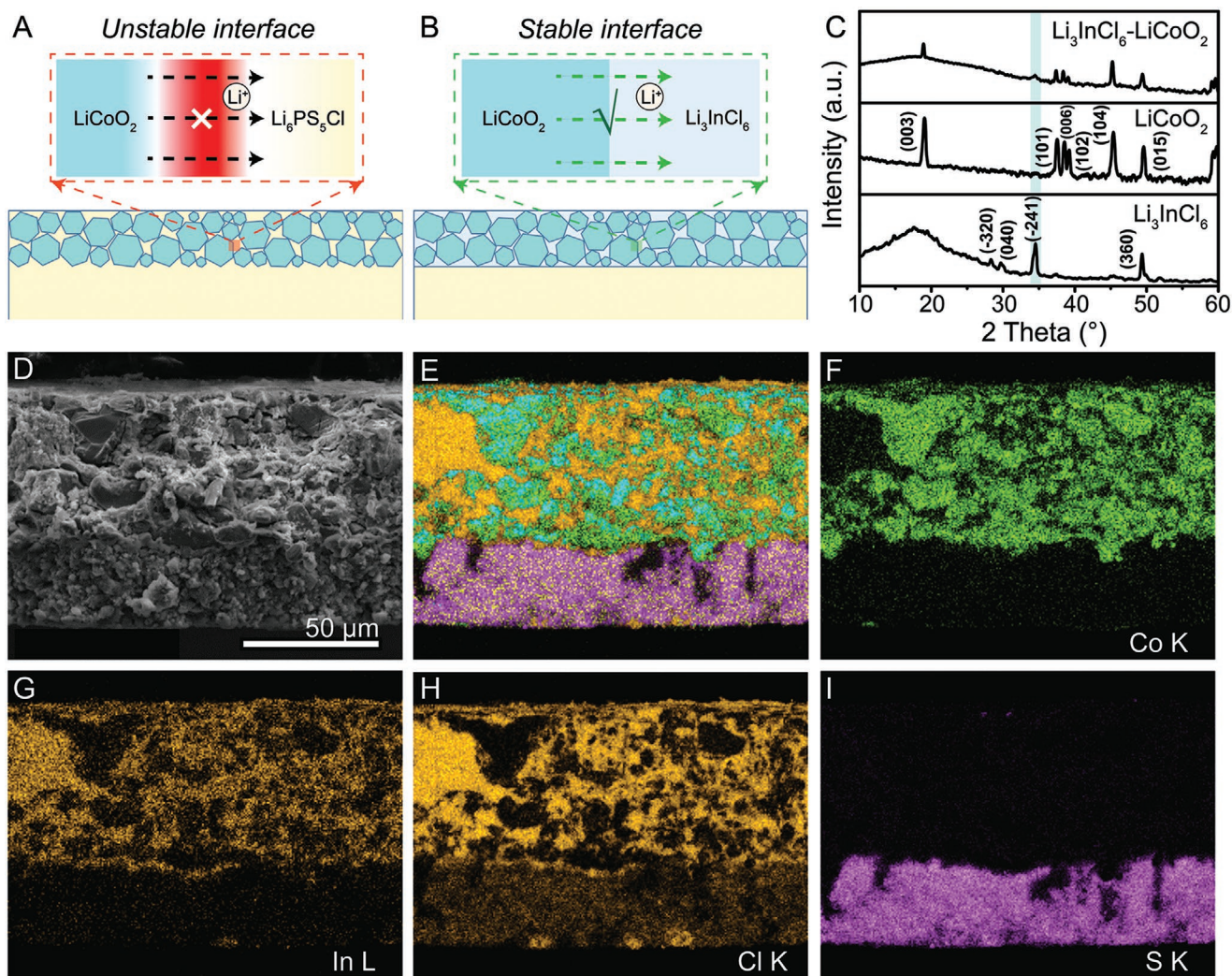


**Figure 5.** Stabilization of the cathode layer. Schematics to illustrate A) the sluggish ion transfer at the  $\text{LiCoO}_2/\text{Li}_6\text{PS}_5\text{Cl}$  interface caused by the side reaction (the red region represents newborn interphase with high resistance), B) the excellent compatibility at the  $\text{LiCoO}_2/\text{Li}_3\text{InCl}_6$  interface induced fast ion transfer. C) XRD spectra of pure  $\text{Li}_3\text{InCl}_6$ ,  $\text{LiCoO}_2$ , and  $\text{Li}_3\text{InCl}_6\text{-LiCoO}_2$  composites. D) Cross-sectional SEM image of the cathode-SE layers. EDS mapping of E) overall elements, F) Co, G) In, H) Cl, I) S in the cross section of the cathode-SE layers.

the  $\text{LiCoO}_2\text{-Li}_3\text{InCl}_6$  composites with that of pure  $\text{LiCoO}_2$  and  $\text{Li}_3\text{InCl}_6$ . The peaks located at  $19.1^\circ$ ,  $37.4^\circ$ ,  $38.4^\circ$ ,  $39.0^\circ$ ,  $45.2^\circ$ , and  $49.5^\circ$  are attributed to the (003), (101), (005), (102), (104), and (015) planes of  $\text{LiCoO}_2$ , respectively. The highlighted one is indexed to the (-241) plane of  $\text{Li}_3\text{InCl}_6$ . No extra peaks appear, suggesting excellent compatibility between  $\text{LiCoO}_2$  and  $\text{Li}_3\text{InCl}_6$ .

In the ASLB fabrication process, the as-prepared cathode powders were further ground and pressed into the thin SE membrane. The mass loading of active material ( $\text{LiCoO}_2$ ) is  $15.9 \text{ mg cm}^{-2}$ . The weight ratio of  $\text{LiCoO}_2$  to  $\text{Li}_3\text{InCl}_6$  is 80:20. Figure 5D-I displays the cross-sectional SEM images and the corresponding EDS element mappings (Co, In, Cl, and S) of the pressed SE-cathode layers, respectively. The cathode layer has a thickness of  $55 \mu\text{m}$ , where  $\text{LiCoO}_2$  particles are uniformly mixed with  $\text{Li}_3\text{InCl}_6$ .

We further evaluated the effects of replacing sulfide with halide in the cathode layer and reducing the thickness of the SE

layer in the ASLBs. As depicted in Figure 6A-C, three cells coupling  $\text{LiCoO}_2\text{-Li}_6\text{PS}_5\text{Cl}$  with thick SE (cell-1),  $\text{LiCoO}_2\text{-Li}_3\text{InCl}_6$  with thick SE (cell-2), and  $\text{LiCoO}_2\text{-Li}_3\text{InCl}_6$  with thin SE (cell-3) were assembled. The mass loading of the whole cathode and active material ( $\text{LiCoO}_2$ ) were  $19.84$  and  $15.87 \text{ mg cm}^{-2}$ , respectively. To avoid the side effect caused by the anode side, In-Li acted as anode material in all three cells. All three cells were tested with a constant current/constant voltage protocol between 2.0 and 4.2 V (vs. In-Li). Figure 6D displays the charge/discharge profiles of three cells at the current rate of  $C/20$ . Impressively, cell-3 (using thin SE and  $\text{LiCoO}_2\text{-Li}_3\text{InCl}_6$  cathode) has the highest discharge capacity of  $172 \text{ mAh g}^{-1}$  and the initial Coulombic efficiency of 98.3%. In comparison, cell-2 (using thick SE and  $\text{LiCoO}_2\text{-Li}_3\text{InCl}_6$  cathode) has a discharge capacity of  $163 \text{ mAh g}^{-1}$  and an initial Coulombic efficiency of 95.9%. The enhanced cell capacity and Coulombic efficiency result from the reduced internal resistance derived from the layer thickness reduction. Meanwhile, it is not surprising that

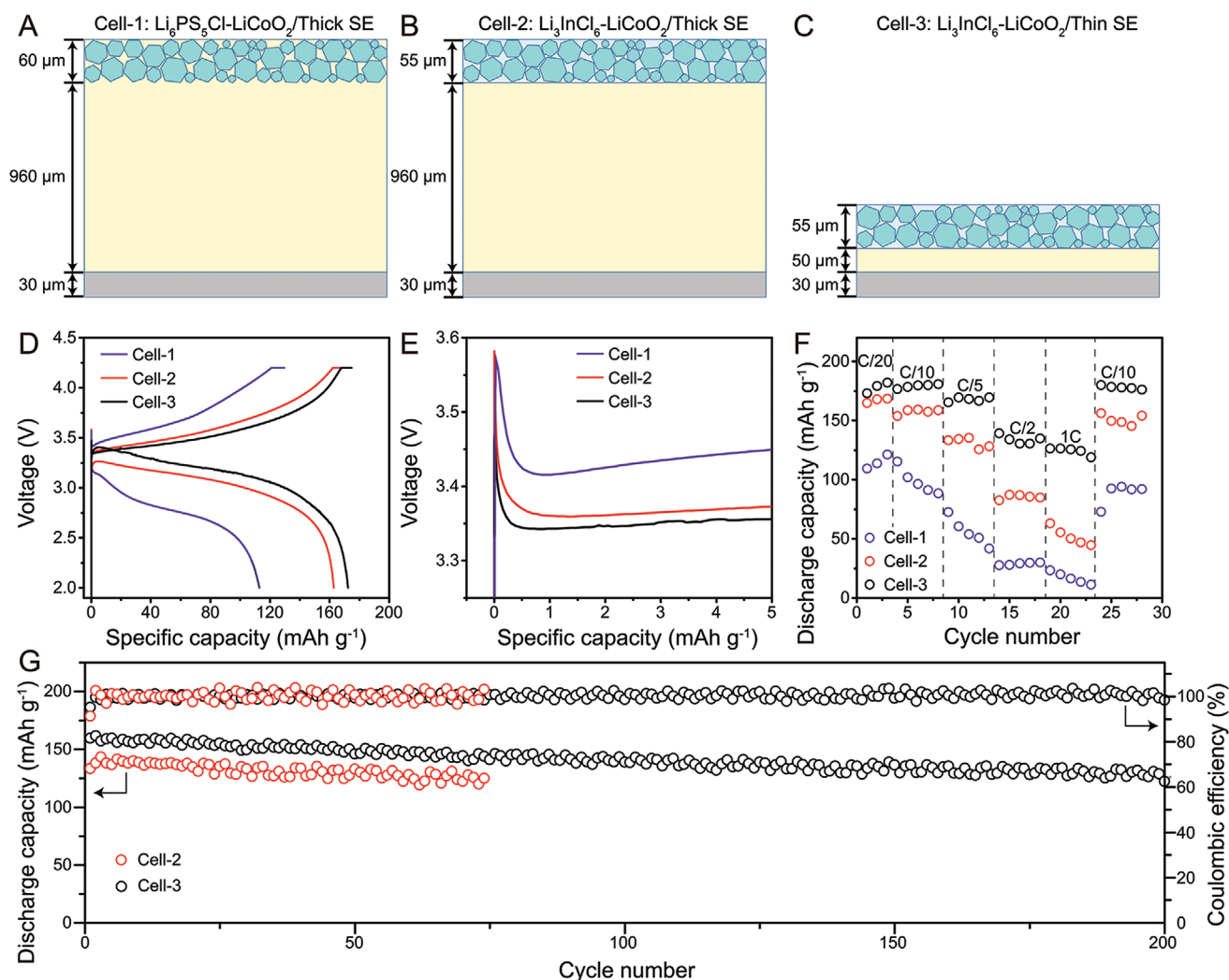


**Figure 6.** Performance of ASLBs. Schematics of the cell architecture of A)  $\text{Li}_6\text{PS}_5\text{Cl-LiCoO}_2/\text{thick SE}$ , B)  $\text{Li}_3\text{InCl}_6\text{-LiCoO}_2/\text{thick SE}$ , and C)  $\text{Li}_3\text{InCl}_6\text{-LiCoO}_2/\text{thin SE}$ . D) Charge/discharge profiles and E) the amplified charge profile of three cells in the first cycle. F) Rate performances of three cells. G) Long-term cycling stabilities of cell-2 and cell-3 at C/5 in room temperature.

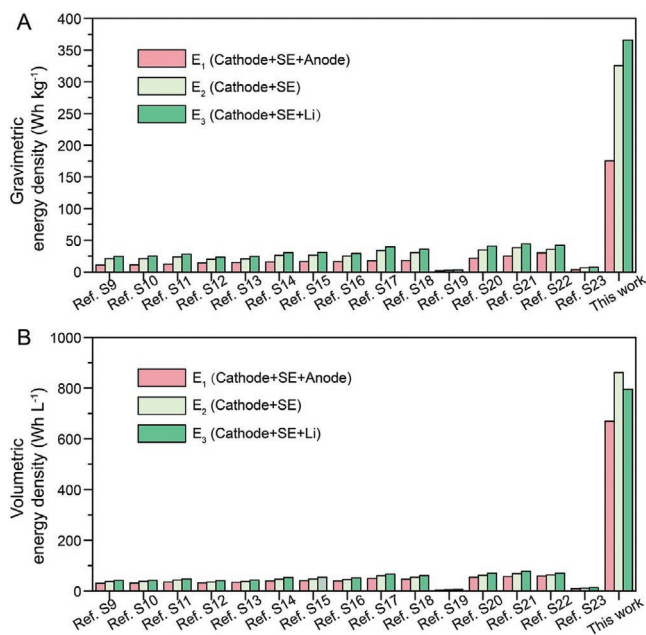
cell-1 (using thick SE and  $\text{LiCoO}_2\text{-Li}_6\text{PS}_5\text{Cl}$ ) had the lowest capacity of  $112 \text{ mAh g}^{-1}$  and the initial Coulombic efficiency of 87.0%, which was because of the side reaction between sulfide and  $\text{LiCoO}_2$ . Figure 6E amplifies the charge profiles of three cells in the initial cycle. The charge potential in cell-2 is 55 mV lower than that of cell-1, demonstrating the enhanced stability of  $\text{Li}_3\text{InCl}_6$  against  $\text{LiCoO}_2$  compared with  $\text{Li}_6\text{PS}_5\text{Cl}$ . Moreover, there is a 20 mV lower potential in cell-3 than that of cell-2, suggesting the lower internal resistance.

Figure 6F compares the rate performances of three cells. Cell-3 exhibits rate capacities of 178, 179, 165, 134, and  $124 \text{ mAh g}^{-1}$  (on average) at the current rates of C/20, C/10, C/5, C/2, and 1C, respectively (1C equals  $200 \text{ mA g}^{-1}$ ). Moreover, the capacity recovers to  $177 \text{ mAh g}^{-1}$  when recharged at C/10, demonstrating an outstanding rate performance. In comparison, cell-2 delivers similar capacity at low rates but greatly reduced capacities at high rates ( $101 \text{ mAh g}^{-1}$  at C/2, and  $58 \text{ mAh g}^{-1}$  at 1C). The remarkably boosted rate performance in cell-3 is attributed to the reduced internal resistance

(or enhanced ion conductance) caused by thinning the SE layer. The high resistance caused by the side reaction between  $\text{LiCoO}_2$  and  $\text{Li}_6\text{PS}_5\text{Cl}$  explains the poor behavior of cell-1 at a high rate (only  $25 \text{ mAh g}^{-1}$  at 1C). Figure 6G shows the long-term cycling performances of cell-2 and cell-3 at the current rate of C/5. Cell-3 exhibits a remarkable initial capacity of  $160 \text{ mAh g}^{-1}$  and maintained stability for 200 cycles with a capacity retention of 82%. The Coulombic efficiency is higher than 99.8%. In contrast, cell-2 shows a lower initial capacity of  $147 \text{ mAh g}^{-1}$ . The environmental temperature variation causes the regular capacity vibration in both cells. The capacity vibration in cell-3 is more moderate than in cell-2, which follows that the ionic conductance of thin SE has lower temperature dependence than that of thick SE.

The gravimetric and volumetric energy densities of cell-3 were evaluated and compared with other reported ASLBs using  $\text{LiCoO}_2$  cathode, sulfide SEs, and In (or In-Li) anode, as depicted in Figure 7. The energy densities are calculated according to the weight and volume of the sum of the





**Figure 7.** Energy densities evaluation. A) Gravimetric and B) volumetric energy densities of cell-3 at  $E_1$  (cathode, SE, and anode),  $E_2$  (cathode and SE), and  $E_3$  (cathode, SE, and Li metal) levels in comparison with other reported ASLBs using  $\text{LiCoO}_2$  cathode, sulfide SE, and In (or In–Li) anode.

following: 1) cathode, SE, and anode ( $E_1$ ); and 2) only cathode and SE ( $E_2$ ).  $E_3$  is calculated as the perspective energy densities of cell-3 when employing Li metal anode. The detailed information on the energy density calculation is listed in Tables S4 and S5 (Supporting Information). Cell-3 delivered remarkable  $E_1$  energy densities ( $175 \text{ Wh kg}^{-1}$ ,  $670 \text{ Wh L}^{-1}$ ) far exceeding than that of other ASLBs ( $<30 \text{ Wh kg}^{-1}$ ,  $<60 \text{ Wh L}^{-1}$ ). The significant difference is highly related to replacing a thick SE pellet with a thin SE membrane. Considering that In anode is generally considered unfeasible for practical ASLBs, the  $E_2$  energy densities that exclude the In anode weight in the calculation are discussed. As a result, cell-3 delivered an ultrahigh gravimetric energy density of  $325 \text{ Wh kg}^{-1}$  and a volumetric energy density of  $861 \text{ Wh L}^{-1}$ . Furthermore, the perspective  $E_3$  energy densities of cell-3 reach  $366 \text{ Wh kg}^{-1}$  and  $795 \text{ Wh L}^{-1}$ , respectively, attributing to the high energy density of Li metal. The critical current density (CCD) of the thin SE membrane when coupled with Li metal is investigated and compared with the thick SE. Figure S14 (Supporting Information) displays the voltage profiles of these two symmetric cells during plating/stripping at a fixed capacity of  $0.1 \text{ mAh cm}^{-2}$ , but a step increased current density from  $0.1$  to  $0.6 \text{ mA cm}^{-2}$ . Overall, the thin SE cell delivers a critical current density of  $0.5 \text{ mA cm}^{-2}$ , the same as the thick SE cell. It demonstrates that the thickness of the SE has a limited effect on its stability with Li metal. In addition, the overpotentials in thin SE are much lower than in thick SE, evidencing the much higher ion conductance in thin SE.

### 3. Conclusions

The significance of developing a thin and highly ion-conductive SE membrane (thickness  $< 50 \mu\text{m}$ , ionic conductivity

$> 1.0 \text{ mS cm}^{-1}$ ) has attracted global interest in both academia and industries, but a few works have achieved this number. Sulfide SEs are one of the most promising SEs to provide superior ion conductivity. However, the challenge in fabricating sulfide-based thin composite membrane is to find a binder that is compatible with sulfide SE, dissolvable in nonpolar solvent, thermally stable, and has high binding strength, and has excellent film formability. Although nonpolar solvents are preferred for sulfide SEs to avoid the degradation of sulfide SEs, most binders are insoluble in nonpolar solvents. The ethyl cellulose in this work satisfies the following requirements: 1) excellent solubility and stability in the nonpolar solvent of toluene; 2) high chemical and electrochemical stability with sulfide SE; 3) outstanding thermal stability; 4) high binding strength; 5) efficient dispersing capability; and (6) excellent membrane formability. Based on the unique amphiphatic molecular structure and the abovementioned merits of ethyl cellulose, we fabricated a flexible, ultrathin, and robust SE membrane through a scalable filtration method. Meanwhile,  $\text{Li}_3\text{InCl}_6$  acted as an interfacial stabilizer and ion conductor for  $\text{LiCoO}_2$  cathode, promoting the reaction kinetic and long-term cycling stability. The reported sulfide SE membrane had a low thickness of  $47 \mu\text{m}$ , a lightweight of  $7.9 \text{ mg cm}^{-2}$ , a superior ionic conductivity of  $1.65 \text{ mS cm}^{-1}$ , an ultralow areal resistance of  $4.32 \Omega \text{ cm}^2$ , an ultrahigh ion conductance of  $291 \text{ mS}$ , remarkable compression robustness under a pressure of  $80 \text{ MPa}$ , and excellent flexibility. The ASLBs employing this thin SE membrane delivered outstanding energy densities of  $325 \text{ Wh kg}^{-1}$  and  $861 \text{ Wh L}^{-1}$  based on cathode and SE layer, and cell-level energy densities of  $175 \text{ Wh kg}^{-1}$  and  $670 \text{ Wh L}^{-1}$ . This work discovered a unique binder for large-scale manufacturing of ultrathin, robust, and highly ionic conductive SE membrane for cell-level high-energy ASLBs.

### 4. Experimental Section

**Materials Synthesis:** The synthesis of  $\text{Li}_6\text{PS}_5\text{Cl}$  was based on the previous work.<sup>[23]</sup> Briefly,  $\text{Li}_2\text{S}$  (Sigma–Aldrich, 99.98%),  $\text{P}_2\text{S}_5$  (Sigma–Aldrich, 99%), and  $\text{LiCl}$  (Sigma–Aldrich, 99%) were stoichiometrically mixed through a ball milling for 10 h at 500 rpm. After that, the mixture was sealed in a glass tube and annealed at  $550 \text{ }^\circ\text{C}$  for 6 h. The collected powder was the raw  $\text{Li}_6\text{PS}_5\text{Cl}$ . Next, the raw  $\text{Li}_6\text{PS}_5\text{Cl}$  was dispersed in toluene and experienced another ball milling process for 5 h at 400 rpm to achieve more fine particles. Finally, after a  $200 \text{ }^\circ\text{C}$  treatment in Ar, the fine  $\text{Li}_6\text{PS}_5\text{Cl}$  powders were obtained.

The  $\text{Li}_3\text{InCl}_6$  was prepared through an as-reported water-mediated approach.<sup>[32]</sup> First, stoichiometric  $\text{InCl}_3$  (Sigma–Aldrich, 99.999%) and  $\text{LiCl}$  (Sigma–Aldrich, 99%) were dissolved in water in sequence. The mixture was then transferred to an oven and heated at  $100 \text{ }^\circ\text{C}$  until the most visible water was removed. After that, the collected powders were further annealed at  $200 \text{ }^\circ\text{C}$  for 7 h in a vacuum to remove the water to get the as-prepared  $\text{Li}_3\text{InCl}_6$ .

The preparation of the  $\text{Li}_3\text{InCl}_6$ – $\text{LiCoO}_2$  mixture was similar to the synthesis of  $\text{Li}_3\text{InCl}_6$ , as mentioned above. The  $\text{LiCoO}_2$  powders (Rogers Inc.) were added into the as-prepared solution of  $\text{InCl}_3$  and  $\text{LiCl}$  in a weight ratio of 80:20. Before removing the water at  $100 \text{ }^\circ\text{C}$  in an oven, the mixture was first treated in a bath sonication for 10 min. After the same water removal processes, the  $\text{Li}_3\text{InCl}_6$ – $\text{LiCoO}_2$  mixture was transferred into the glovebox and stored for future use.

**$\text{Li}_6\text{PS}_5\text{Cl}$ –Ethyl Cellulose Membrane Fabrication:** A vacuum filtration method was employed to prepare the thin membranes, conducted in



the glovebox. Briefly, 2 mg of ethyl cellulose was first dissolved in 1 mL of toluene. After that, 98 mg of fine  $\text{Li}_6\text{PS}_5\text{Cl}$  powders were added to the ethyl cellulose solution, accompanied by continuous mechanical stirring to achieve uniform dispersion. The dispersion was then cast in the vacuum filtration system. A freestanding thin membrane can be obtained after peeling it off from the filter paper. The membrane was then sandwiched between two glass slides and heated at 150 °C for 12 h on a hot plate to remove the toluene completely. A commercial separator (Celgard 2400) was utilized as the filter paper due to limited pore size (43 nm). A coarse-frit glass filter (Fisher Scientific) with a diameter of 47 mm was used in the filtration process.

**Materials Characterization:** The XRD was conducted on PANalytical/Philips X'Pert Pro (PANalytical, Netherlands) with  $\text{Cu K}\alpha$  radiation. The Raman spectra were measured on a Thermo Scientific DXR (Thermo Scientific, USA) with 532 nm laser excitation. The samples were sealed with Kapton tape to avoid exposure to air. The SEM and EDS were characterized by SEM JEOL JSM 7000F (JEOL Ltd., Japan). The FTIR was measured on JASCO FT/IR-6600 (JASCO International Co., Ltd., USA). The viscosity was performed on Discovery Hybrid Rheometer HR 30 (TA Instruments, USA). The concentrations of cellulose, ethyl cellulose,  $\text{Li}_6\text{PS}_5\text{Cl}$ ,  $\text{Li}_6\text{PS}_5\text{Cl}$ -cellulose, and  $\text{Li}_6\text{PS}_5\text{Cl}$ -ethyl cellulose were 2, 2, 100, 98/2, and 98/2 mg mL<sup>-1</sup> in toluene, respectively. The compression strength was conducted on a Zwick/Roell material testing machine (ZwickRoell, USA). The thin SE membrane was cut into a circular shape with a diameter of 1/2 in. and a thickness of 0.05 mm. The thick SE pellet with the same diameter but thickness of 1 mm was prepared through a cold-press method. The displacement speed was 0.001 mm s<sup>-1</sup>. The tensile strength test was carried out by using a HR 30 Discovery Hybrid Rheometer-dynamic mechanical analysis (DMA) (TA Instruments, USA). The thin SE membrane was cut into a size of 3 cm in length and 5 mm in width. The displacement speed was set at 0.01 mm s<sup>-1</sup>.

**X-Ray Computed Tomography:** For the XCT measurement, a Zeiss Xradia Versa 520 XCT unit was used, which was operated at 30 kV and 68  $\mu\text{A}$ . For increased magnification and resolution, a 4 $\times$  scintillator objective was used in front of the CCD camera. A 2  $\times$  2 binning (on the detector) was used for optimized measurement time and resolution; resulting in a  $x = y = z = 2.46 \mu\text{m}$  pixel size. XCT data were collected over a sample rotation of  $\omega = 360^\circ$  with 1601 projections at equal steps. For image processing and segmentation, the ORS Dragonfly PRO v.3.5 software was used.

**Electrochemical Characterization:** The ionic conductivities of  $\text{Li}_6\text{PS}_5\text{Cl}$  powder,  $\text{Li}_6\text{PS}_5\text{Cl}$ -ethyl cellulose membrane, and  $\text{Li}_3\text{InCl}_6$  powder were measured using electrochemical impedance spectroscopy (EIS) by symmetric systems with different ion-blocking electrodes. The ionic conductivity measurement of  $\text{Li}_6\text{PS}_5\text{Cl}$  powder could be found in the previous work.<sup>[23]</sup> The  $\text{Li}_6\text{PS}_5\text{Cl}$ -ethyl cellulose membrane was first cut into a 12.7 mm circular sheet and then pressed under 300 MPa in a 12.7 mm polyether ether ketone (PEEK) die. Two pieces of indium foils (30  $\mu\text{m}$  in thickness and 11.1 mm in diameter) were pressed onto two stainless steel plugs and then attached on both sides of the  $\text{Li}_6\text{PS}_5\text{Cl}$ -ethyl cellulose membrane in the die under 10 MPa. The total die with plugs was fixed in a stainless steel framework to conduct EIS directly. The ionic conductivity of  $\text{Li}_3\text{InCl}_6$  was measured under similar processes with  $\text{Li}_6\text{PS}_5\text{Cl}$  except using stainless steel foil as electrodes to avoid the side reaction between indium and  $\text{Li}_3\text{InCl}_6$ .

**Fabrication of ASLB Using Thick SE:** The ASLB fabrication with thick SE was conducted in the glovebox. First, 200 mg of  $\text{Li}_6\text{PS}_5\text{Cl}$  powders was pressed in a PEEK die with a diameter of 12.7 mm under 300 MPa. Then 25 mg of as-prepared  $\text{Li}_3\text{InCl}_6$ - $\text{LiCoO}_2$  mixture was cast and then pressed on one side of the  $\text{Li}_6\text{PS}_5\text{Cl}$  under 100 MPa. A piece of In-Li was pressed on the other side with a pressure of 100 MPa to work as an anode. The Cu and stainless steel foil were selected as current collectors for anode and cathode, respectively. Finally, an extra pressure of 50 MPa was applied to the cell and maintained with a stainless steel framework.

**Fabrication of ASLB Using Thin SE:** The fabrication of ASLB using thin SE was similar to the fabrication of thick SE as aforementioned. A piece

of In-Li foil was first pressed on the stainless steel plug with a diameter of 12.6 mm under a pressure of 300 MPa. After that, a 12.7 mm circular thin SE membrane was pressed on the In-Li foil in a PEEK die under 300 MPa. Then 25 mg of  $\text{Li}_3\text{InCl}_6$ - $\text{LiCoO}_2$  was cast on the top of thin SE and further pressed under 100 MPa. Finally, an extra pressure of 50 MPa was applied to the cell and maintained with a stainless steel framework.

**Rate and Cycling Performance:** The rate and cycling measurement were conducted with a protocol that the cell was charged at constant current to 4.2 V, held at 4.2 V for 1 h, and then discharged to 2.5 V at a constant current. The current was calculated based on the mass and capacity of cathode active material. The rate performance was measured at C/20 for the first three cycles; then C/10, C/5, C/2, and 1C for five cycles, respectively; and finally recovered to C/20 for another five cycles. Long-term cycling was conducted at C/5. Here 1C means 200 mA g<sup>-1</sup> based on the weight of cathode active material.

## Supporting Information

Supporting Information is available from the Wiley Online Library or from the author.

## Acknowledgements

H.Z. acknowledges the financial support from National Science Foundation under Award Number CBET-ES-1924534 and Rogers Corporation. S.O. and X.Z. acknowledge the support from the US Department of Energy (DOE), Office of Energy Efficiency and Renewable Energy, Advanced Manufacturing Office. The authors would like to acknowledge Dr. Yaning Li and Dr. Tiantian Li in the Department of Mechanical and Industry Engineering at Northeastern University for the help with compression measurement and the Northeastern University Center for Renewable Energy Technology for the use of SEM facilities. This paper was authored in part by UT-Battelle LLC under contract DE-AC05-00OR22725 with DOE. The US government retains and the publisher, by accepting the article for publication, acknowledges that the US government retains a nonexclusive, paid-up, irrevocable, worldwide license to publish or reproduce the published form of this manuscript, or allow others to do so, for US government purposes. DOE will provide public access to these results of federally sponsored research in accordance with the DOE Public Access Plan (<http://energy.gov/downloads/doe-public-access-plan>).

## Conflict of Interest

The authors declare no conflict of interest.

## Author Contributions

H.Z. conceived the idea. D.C. carried out the main experiments. X.S. did SEM characterization. Y.W. did FTIR characterization. Q.L. did viscosity test. X.Z., E.C., and S.O. performed the XCT characterization and analysis. W.L. helped the TEM characterization via EDX mapping. D.C. and H.Z. wrote the paper. A.A. polished the language. All authors commented on the final manuscript.

## Data Availability Statement

Research data are not shared.

## Keywords

all-solid-state batteries, binders, cathode stabilization, cell-level energy density, ion conductive membranes, sulfide electrolytes

Received: July 16, 2021

Revised: September 24, 2021

Published online:

- [1] a) X. Feng, M. Ouyang, X. Liu, L. Lu, Y. Xia, X. He, *Energy Storage Mater.* **2018**, *10*, 246; b) D. Zhou, Y.-B. He, R. Liu, M. Liu, H. Du, B. Li, Q. Cai, Q.-H. Yang, F. Kang, *Adv. Energy Mater.* **2015**, *5*, 1500353.
- [2] Z. P. Cano, D. Banham, S. Ye, A. Hintennach, J. Lu, M. Fowler, Z. Chen, *Nat. Energy* **2018**, *3*, 279.
- [3] Q. Zhang, D. Cao, Y. Ma, A. Natan, P. Aurora, H. Zhu, *Adv. Mater.* **2019**, *31*, 1970311.
- [4] K. J. Kim, M. Balaish, M. Wadaguchi, L. Kong, J. L. M. Rupp, *Adv. Energy Mater.* **2021**, *11*, 2002689.
- [5] D. Cao, X. Sun, Q. Li, A. Natan, P. Xiang, H. Zhu, *Matter* **2020**, *3*, 57.
- [6] D. Cao, Y. Zhao, X. Sun, A. Natan, Y. Wang, P. Xiang, W. Wang, H. Zhu, *ACS Energy Lett.* **2020**, *5*, 3468.
- [7] J. Schnell, T. Günther, T. Knoche, C. Vieider, L. Köhler, A. Just, M. Keller, S. Passerini, G. Reinhart, *J. Power Sources* **2018**, *382*, 160.
- [8] S. Randau, D. A. Weber, O. Kötz, R. Koerver, P. Braun, A. Weber, E. Ivers-Tiffée, T. Adermann, J. Kulisch, W. G. Zeier, F. H. Richter, J. Janek, *Nat. Energy* **2020**, *5*, 259.
- [9] J. Wu, L. Yuan, W. Zhang, Z. Li, X. Xie, Y. Huang, *Energy Environ. Sci.* **2021**, *14*, 12.
- [10] a) Y.-G. Lee, S. Fujiki, C. Jung, N. Suzuki, N. Yashiro, R. Omoda, D.-S. Ko, T. Shiratsuchi, T. Sugimoto, S. Ryu, J. H. Ku, T. Watanabe, Y. Park, Y. Aihara, D. Im, I. T. Han, *Nat. Energy* **2020**, *5*, 299; b) W. Ping, C. Wang, R. Wang, Q. Dong, Z. Lin, A. H. Brozena, J. Dai, J. Luo, L. Hu, *Sci. Adv.* **2020**, *6*, eabc8641.
- [11] D. H. Kim, Y.-H. Lee, Y. B. Song, H. Kwak, S.-Y. Lee, Y. S. Jung, *ACS Energy Lett.* **2020**, *5*, 718.
- [12] a) Y. J. Nam, D. Y. Oh, S. H. Jung, Y. S. Jung, *J. Power Sources* **2018**, *375*, 93; b) D. Y. Oh, Y. J. Nam, K. H. Park, S. H. Jung, K. T. Kim, A. R. Ha, Y. S. Jung, *Adv. Energy Mater.* **2019**, *9*, 1802927.
- [13] H. Zhu, W. Luo, P. N. Ciesielski, Z. Fang, J. Y. Zhu, G. Henriksson, M. E. Himmel, L. Hu, *Chem. Rev.* **2016**, *116*, 9305.
- [14] G. S. Rekhi, S. S. Jambhekar, *Drug Dev. Ind. Pharm.* **1995**, *21*, 61.
- [15] P. Ahmadi, A. Jahanban-Esfahlan, A. Ahmadi, M. Tabibiazar, M. Mohammadifar, *Food Rev. Int.* **2020**, *1*.
- [16] L. W. McKeen, in *Film Properties of Plastics and Elastomers*, 3rd ed. (Ed: L. W. McKeen), William Andrew Publishing, Boston, MA **2012**, p. 353.
- [17] R. Giernoth, in *Solvents and Solvent Effects in Organic Chemistry*, (Eds: C. Reichardt, T. Welton), Wiley VCH, Weinheim **2010**, p. 509.
- [18] V. Hospodarova, E. Singovszka, N. Stevulova, *Am. J. Anal. Chem.* **2018**, *9*, 303.
- [19] X. Wu, L. Zhang, X. Zhang, Y. Zhu, Y. Wu, Y. Li, B. Li, S. Liu, J. Zhao, Z. Ma, *Sci. Rep.* **2017**, *7*, 12079.
- [20] F. J. Simon, M. Hanauer, F. H. Richter, J. Janek, *ACS Appl. Mater. Interfaces* **2020**, *12*, 11713.
- [21] Y. E. Aimene, J. A. Nairn, *Wood Sci. Technol.* **2015**, *49*, 21.
- [22] M. Xuan, W. Xiao, H. Xu, Y. Shen, Z. Li, S. Zhang, Z. Wang, G. Shao, *J. Mater. Chem. A* **2018**, *6*, 19231.
- [23] D. Cao, Y. Zhang, A. M. Nolan, X. Sun, C. Liu, J. Sheng, Y. Mo, Y. Wang, H. Zhu, *Nano Lett.* **2019**, *20*, 1483.
- [24] T. Yersak, J. R. Salvador, R. D. Schmidt, M. Cai, *ACS Appl. Energy Mater.* **2019**, *2*, 3523.
- [25] J. A. Lewis, F. J. Q. Cortes, Y. Liu, J. C. Miers, A. Verma, B. S. Vishnugopi, J. Tippens, D. Prakash, T. S. Marchese, S. Y. Han, C. Lee, P. P. Shetty, H.-W. Lee, P. Shevchenko, F. De Carlo, C. Saldana, P. P. Mukherjee, M. T. McDowell, *Nat. Mater.* **2021**, *20*, 503.
- [26] Z. Ning, D. S. Jolly, G. Li, R. De Meyere, S. D. Pu, Y. Chen, J. Kasemchainan, J. Ihli, C. Gong, B. Liu, D. L. R. Melvin, A. Bonnin, O. Magdysyuk, P. Adamson, G. O. Hartley, C. W. Monroe, T. J. Marrow, P. G. Bruce, *Nat. Mater.* **2021**, *20*, 1121.
- [27] J.-M. Doux, Y. Yang, D. H. S. Tan, H. Nguyen, E. A. Wu, X. Wang, A. Banerjee, Y. S. Meng, *J. Mater. Chem. A* **2020**, *8*, 5049.
- [28] L. Wang, B. Chen, J. Ma, G. Cui, L. Chen, *Chem. Soc. Rev.* **2018**, *47*, 6505.
- [29] N. Ohta, K. Takada, L. Zhang, R. Ma, M. Osada, T. Sasaki, *Adv. Mater.* **2006**, *18*, 2226.
- [30] X. Li, J. Liang, X. Yang, K. R. Adair, C. Wang, F. Zhao, X. Sun, *Energy Environ. Sci.* **2020**, *13*, 1429.
- [31] C. Wang, J. Liang, M. Jiang, X. Li, S. Mukherjee, K. Adair, M. Zheng, Y. Zhao, F. Zhao, S. Zhang, R. Li, H. Huang, S. Zhao, L. Zhang, S. Lu, C. V. Singh, X. Sun, *Nano Energy* **2020**, *76*, 105015.
- [32] X. Li, J. Liang, N. Chen, J. Luo, K. R. Adair, C. Wang, M. N. Banis, T.-K. Sham, L. Zhang, S. Zhao, S. Lu, H. Huang, R. Li, X. Sun, *Angew. Chem., Int. Ed. Engl.* **2019**, *58*, 16427.